MitoNEET is a uniquely folded 2Fe–2S outer mitochondrial membrane protein stabilized by pioglitazone

Mark L. Paddock*, Sandra E. Wiley†, Herbert L. Axelrod‡, Aina E. Cohen‡, Melinda Roy§, Edward C. Abresch*, Dominique Capraro§, Anne N. Murphy†, Rachel Nechushtai¶, Jack E. Dixon†§‖, and Patricia A. Jennings§**

Departments of *Physics, †Pharmacology, §Chemistry and Biochemistry, and ‖Cellular and Molecular Medicine, University of California at San Diego, La Jolla, CA 92093; ‡Stanford Synchrotron Radiation Laboratory, 2575 Sand Hill Road, Menlo Park, CA 94025; and ¶Department of Plant and Environmental Sciences, The Wolfson Centre for Applied Structural Biology, Hebrew University of Jerusalem, Givat Ram 91904, Israel

Communicated by Douglas C. Rees, California Institute of Technology, Pasadena, CA, August 1, 2007 (received for review July 9, 2007)

Iron–sulfur (Fe–S) proteins are key players in vital processes involving energy homeostasis and metabolism from the simplest to most complex organisms. We report a 1.5 Å x-ray crystal structure of the first identified outer mitochondrial membrane Fe–S protein, mitoNEET. Two protomers intertwine to form a unique dimeric structure that constitutes a new fold to not only the ≈650 reported Fe–S protein structures but also to all known proteins. We name this motif the NEET fold. The protomers form a two-domain structure: a β-cap domain and a cluster-binding domain that coordinates two acid-labile 2Fe–2S clusters. Binding of pioglitazone, an insulin-sensitizing thiazolidinedione used in the treatment of type 2 diabetes, stabilizes the protein against 2Fe–2S cluster release. The biophysical properties of mitoNEET suggest that it may participate in a redox-sensitive signaling and/or in Fe–S cluster transfer.

diabetes | FeS cluster | iron homeostasis | thiazolidinedione | oxidative stress

Iron (Fe) is a vital trace element for virtually all organisms. Incorporation of this transition metal into iron–sulfur (Fe–S) clusters forms cofactors integral to diverse biological pathways involved in the capture and metabolism of light and chemical energy (1, 2). Because free iron can be highly toxic, an elaborate array of proteins has evolved to facilitate the transfer of iron through cell compartments, to insert iron into Fe–S clusters, and to incorporate Fe–S clusters into proteins. Fe–S cluster assembly takes place primarily, although not exclusively, within the mitochondrial matrix of eukaryotic cells, and defects in mitochondrial cluster assembly and export have profound consequences for rates of growth, iron accumulation, oxidative stress, and heme biosynthesis (1, 2).

Mitochondrial dysfunction is associated with insulin resistance and the development of type 2 diabetes (3). Recent studies suggest that disease pathogenesis involves diminished mitochondrial oxidative capacity in insulin-sensitive tissues. Pharmacologic agents extensively used to treat insulin resistance such as the thiazolidinedione (TZD) pioglitazone are known to enhance oxidative capacity and normalize lipid metabolism (4, 5). Although TZDs are conventionally thought to operate through binding to peroxisome proliferator-activated receptors, a recent study by Colca and colleagues (6) identified an additional binding target within mitochondrial membranes that was named mitoNEET, on the basis of the subcellular localization (mito) and the presence of the amino acid sequence Asn-Glu-Glu-Thr (NEET).

MitoNEET was determined to be an integral protein of the outer mitochondrial membrane (OMM) by a series of studies, including immuno-electron microscopy and detailed fractionation studies of highly purified rat liver mitochondria. An amino-terminal signal sequence within the first 32 residues, containing a predicted transmembrane domain, targets mitoNEET to the outer membrane. The orientation of this protein toward the cytoplasm was established by proteolytic digestion of this protein on intact rat liver mitochondria. Deficiency of this protein in mice results in a compromise in the respiratory capacity of heart mitochondria (7).

MitoNEET belongs to an ancient family of proteins for which the hallmark is the presence of a unique 39-aa CDGSH domain [consensus sequence C-X-C-X2-(S/T)-X3-P-X-C-D-G-(S/A/T)-H]. Although currently annotated as a zinc finger moiety in the NCBI protein database (8), the CDGSH domain actually binds a 2Fe–2S cluster. As such, mitoNEET is the first identified 2Fe–2S cluster containing protein located on the OMM (7, 9). The absorption spectrum has a peak near 460 nm attributed to the 2Fe–2S cluster that is reversibly reduced by dithionite and oxygen. The cluster is labile at pH ≤8.0, as shown by the loss of the spectral signature and of the 2Fe and 2S as shown by mass spectroscopy (9). We report that this novel OMM protein folds into a unique homodimeric structure with one 2Fe–2S cluster bound to each protomer within the dimer determined by x-ray crystallography using multiwavelength anomalous dispersion (MAD) phasing.

Results

The Overall Unique Structure and Domain Topology of MitoNEET. In an effort to understand the structural properties of this protein, we produced a soluble form of recombinant human mitoNEET corresponding to amino acids 33–108 (lacking the amino-terminal targeting and transmembrane sequences) for structural analysis. The isolated recombinant protein crystallized in the orthorhombic space group $P2_12_12_1$, with unit-cell parameters a = 46.81 Å, b = 49.62 Å, c = 59.01 Å. The Matthews coefficient (V_m) of the crystal was 1.9 Å^3/Da with an estimated solvent content of 33%.

We determined the crystal structure of mitoNEET by MAD phasing (10). X-ray diffraction intensities were collected at Stanford Synchrotron Radiation Laboratory (SSRL) BL9-2 to a resolution of 1.8 Å at three wavelengths corresponding to the inflection, absorp-

Author contributions: M.L.P., R.N., J.E.D., and P.A.J. designed research; M.L.P., S.E.W., H.L.A., A.E.C., M.R., E.C.A., D.C., A.N.M., R.N., and P.A.J. performed research; M.L.P., S.E.W., H.L.A., A.E.C., M.R., R.N., and P.A.J. contributed new reagents/analytic tools; M.L.P., S.E.W., H.L.A., A.E.C., M.R., E.C.A., D.C., A.N.M., R.N., J.E.D., and P.A.J. analyzed data; and M.L.P., S.E.W., H.L.A., A.E.C., M.R., E.C.A., A.N.M., R.N., J.E.D., and P.A.J. wrote the paper.

The authors declare no conflict of interest.

Freely available online through the PNAS open access option.

Abbreviations: TZD, thiazolidinedione; OMM, outer mitochondrial membrane; MAD, multiwavelength anomalous dispersion; SSRL, Stanford Synchrotron Radiation Laboratory.

Data Deposition: The atomic coordinates have been deposited in the Protein Data Bank, www.pdb.org (PDB ID code 2QH7).

**To whom correspondence should be addressed at: Department of Chemistry and Biochemistry, University of California at San Diego, 9500 Gilman Drive, La Jolla, CA 92093-0375. E-mail: pajennin@ucsd.edu.

This article contains supporting information online at www.pnas.org/cgi/content/full/0707189104/DC1.

Table 1. Summary of crystal parameters, data collection, and refinement statistics for mitoNEET

Space group		$P2_12_12_1$		
Unit cell parameters		a = 46.81 Å, b = 49.62 Å, c = 59.01 Å		
Data collection	λ_1 MADFe	λ_2 MADFe	λ_3 MADFe	λ_4 native
Wavelength, Å	1.7418	1.3624	1.7374	0.97945
Resolution range, Å	38.21–1.80	29.70–1.80	38.18–1.80	46.83–1.50
No. of observations	150,328	179,865	150,046	604,419
No. of unique reflections	12,904	13,465	12,921	21,479
Completeness, %	95.6 (60.9)*	99.6 (100)	95.9 (63.4)	94.7 (66.8)
Mean I/σ, I	22.3 (1.9)*	33.5 (11.7)	22.1 (2.0)	30.9 (3.2)
R_{sym} on I, %	7.8 (50.4)*	6.6 (19.6)	8 (45.5)	5.8 (75.4)
Highest resolution shell, Å	1.85–1.80	1.85–1.80	1.85–1.80	1.55–1.50
Model and refinement statistics				
Resolution range, Å	46.83–1.50	Data set used in refinement		λ_4 native
No. of reflections (total)	21,479†	Cutoff criteria		$\|F\| > 0$
No. of reflections (test)	1,081	R_{cryst}		0.182
Completeness, % total	94.7	R_{free}		0.223
Stereochemical parameters				
Restraints (RMS observed)				
Bond angle, °		1.72		
Bond length, Å		0.012		
Average isotropic B-value, Å^2		33.3		
ESU based on R_{free}, Å		0.084		

ESU, estimated overall coordinate error (12, 31). $R_{sym} = \Sigma|I_i - \langle I_i\rangle|/\Sigma|I_i|$, where I_i is the scaled intensity of the ith measurement and $\langle I_i\rangle$ is the mean intensity for that reflection. $R_{cryst} = \Sigma|\,|F_{obs}| - |F_{calc}|\,|/\Sigma|F_{obs}|$, where F_{calc} and F_{obs} are the calculated and observed structure factor amplitudes, respectively. $R_{free} = R_{cryst}$, but for 5.0% of the total reflections chosen at random and omitted from refinement.

*Highest-resolution shell in parentheses.

†Typically, the number of unique reflections used in refinement is less than the total number that were integrated and scaled. Reflections are excluded due to systematic absences, negative intensities, and rounding errors in the resolution limits and cell parameters.

tion peak, and high energy remote. X-ray diffraction data from a second crystal were collected to an enhanced resolution of 1.5 Å for refinement of the atomic coordinates (Table 1). The model was refined to an R-factor of 18.2% (R_{free} = 22.2%). The high quality of the electron density is shown in Fig. 1*A*. The refined model reveals a parallel homodimeric structure that includes the cytoplasmic fragment of each protomer from Lys-42 to Lys-106 on Protomer A and from Ala-43 to Glu-107 on Protomer B of the dimer (Fig. 1*A*). The homodimer is tightly packed with 2,020 Å^2 of buried surface area at the interface. Model validation using the MOLPROBITY (12) structure validation tool indicates that 96.8% of the amino acid residues are in the favored region of Φ/Ψ space.

Each protomer is composed of a helical turn (Met-62–Asp-64), an alpha helix (Ala-86–Thr-94), an anti-parallel β-structure (Lys-68–Tyr-71, Leu-101–Lys-104), an additional "swapping" strand (Ile-56–Asp-61), and 11 interconnecting β-turns and loops (Fig. 1). The protein is folded into two spatially distinct subregions: a β-rich or "β-cap" domain and a helical 2Fe–2S binding or "cluster-binding" domain (Fig. 1*B*). Fig. 1 provides a detailed topological analysis of each of these domains. The β-rich domain contains a strand swap from opposite ends of the primary sequence to form the β-cap structure (Fig. 1*B*). This domain contains 28 residues within β-strands with residues Ile-56–Asp-61 from Protomer A and Lys-68–Tyr-71 and Leu-101–Lys-104 from Protomer B making one three-stranded sheet, and with Ile-56–Asp-61 from Protomer B and Lys-68–Tyr-71 and Leu-101–Lys-104 from Protomer A making the second β-sheet (Fig. 1*B*). These two strand-swapped sheets pack together to form the β-cap domain and form the narrowest end (15 Å across) of the structure (Fig. 1*B*). The swapped regions come from opposite ends of the primary sequence (Fig. 1*C*). A prominent feature of the structure is the presence of two 2Fe–2S clusters that are separated by ≈16 Å from each other within the larger helical cluster-binding domain (≈30 Å across) (Fig. 1*B*). The N termini protrude from the bottom of the cluster-binding domain and link to the membrane-spanning sequence (data not shown) in the full-length protein, orienting this domain close to the OMM. A structural similarity search using the DALI server (13) revealed that this fold is novel when compared with the >650 known Fe–S proteins, and it is also unique when compared with the >44,200 known members of the structural databases. Hence we term this structural class the NEET fold.

The Buried Interface Is Unusual in MitoNEET. Molecular representations of mitoNEET are shown in Fig. 2 and highlight the packing of hydrophobic and charged residues. In Fig. 2*A* we show two orientations of the structure. The hydrophobic/aromatic residues predominantly cluster in the center of the molecule and stabilize the individual protomers (Fig. 2*B*). Charged residues cluster at the top of the β-cap domain and at the 2Fe–2S cluster-binding domain (Fig. 2*C*). This distribution creates a dimer that is polar at the top and bottom separated by a hydrophobic region. An interesting asymmetry of charge is located within the interior of the protein forming a macrodipole with the negative end at the top of the β-cap domain and the positive end within the cluster-binding domain, formed by an unexpected interprotomer hydrogen bond between His-58 and Arg-73 located near the cluster (Figs. 2*C* and 3). Interestingly, the conserved Arg-73 is located directly between the Cys ligands of the innermost Fe of the cluster (Fig. 3). This interaction stabilizes the dimer interface. Separating the poles of the dipole are the hydrophobic residues that form a ring around the two protomers within the dimer (Fig. 2*B*). The hydrophobic nature of this area may play a role in flexibility and mobility in the vicinity of the 2Fe–2S cluster contributing to its binding and release.

The 2Fe–2S Cluster Cradle. The sequences Lys-42–Lys-55 and Cys-72–Asn-97 on each protomer comprise the cluster-binding domain (Fig. 1 *B* and *D*). Within the cluster-binding domain, the polypeptide backbone chain from Cys-72–Gly-85 folds into a coil that contains the three coordinating Cys ligands—Cys-72, Cys-74, and Cys-83—and cradles the 2Fe–2S cluster (Fig. 3). The fourth ligand

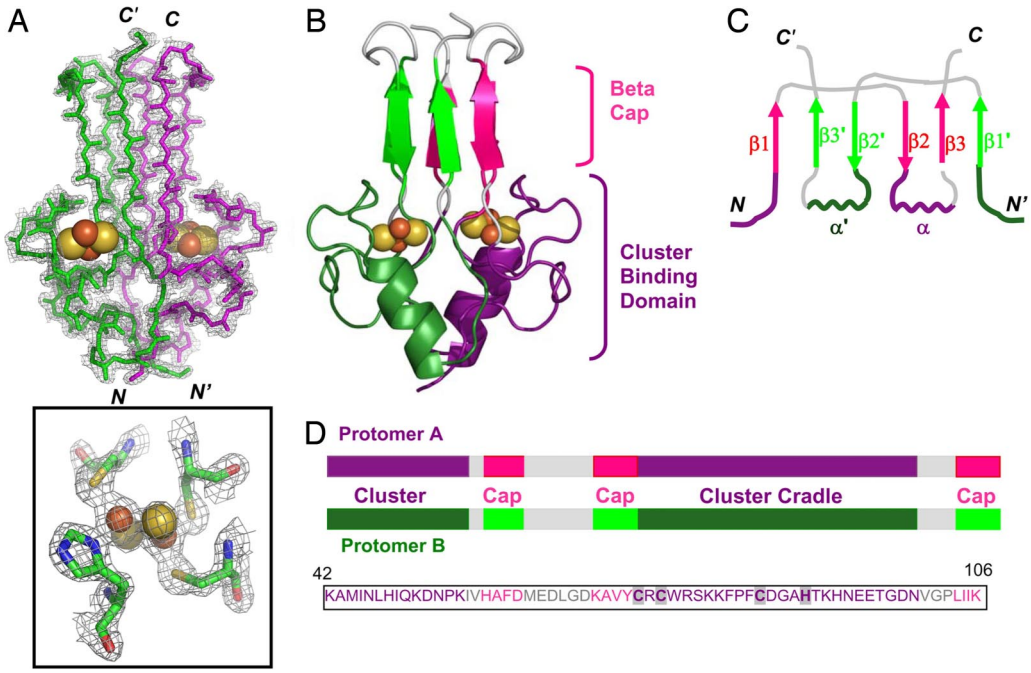

Fig. 1. Overall structural organization and domain topology of dimeric mitoNEET. (*A Upper*) The backbone tracing of each protomer colored in green and magenta, respectively, together with the $2F_o - F_c$ electron density (gray) map contoured at 1.5σ. The protomers pack in a parallel fashion with each protomer harboring a 2Fe–2S cluster, depicted as yellow (sulfur) and red (iron) spheres; N and C termini are indicated. (*Lower*) The box shows an expanded view of one 2Fe–2S cluster (rotated ≈90° from upper view) and ligands and the corresponding $2F_o - F_c$ electron density (gray) map contoured at 2.0σ. (*B*) Ribbon diagram highlighting the two domains of the mitoNEET dimer. A six-stranded β-sandwich forms the intertwined β-cap domain and a larger cluster-binding domain carries two 2Fe–2S clusters. (*C*) A topology diagram highlighting the organization of the secondary structural units (numbered) illustrates the strand swap between protomers. (*D*) Coded segments contributing to each domain are highlighted on the primary sequence and block diagram. Protomer sequences within the cluster-binding domain are colored in purple and dark green, and the sequences corresponding to the β-cap domain are given in pink and light green, respectively. The amino acid sequence of the resolved amino acid strand is shown in the box with the cluster and cap regions colored as for protomer A; the numbers indicate the first (Lys-42) and last (Lys-106) resolved amino acid. The ligands to the 2Fe–2S cluster shown in the expanded boxed view in *A* are indicated in bold and highlighted in gray. The 2Fe–2S binding cradle is located sequentially between two partial β-cap domains. Rendered with Pymol (11).

for the 2Fe–2S cluster (His-87) lies at the N terminus of the α-helix within cluster-binding domain Ala-86-Thr-94. Interestingly, mitoNEET shares this unusual 3Cys cluster coordination with the structurally unrelated cluster scaffold protein IscU (14, 15). The 3Cys–1His coordination seen here is in agreement with the conclusions of previous solution studies of mitoNEET (9). Cys-83 and His-87 are solvent-accessible and coordinate to the outermost Fe, whereas Cys-72 and Cys-74 coordinate the innermost Fe of the 2Fe–2S cluster (Fig. 3). The binding coils, one from each protomer, protrude away from the core of the dimer and the noncrystallographic dyad axis (Fig. 1*A*). We predict that the cluster-binding domain, and specifically the C terminus of each α-helix is situated near the OMM *in vivo*.

Pioglitazone Stabilizes the 2Fe–2S Cluster. Pioglitazone, a member of the TZD class of insulin-sensitizer drugs (16–18), binds to mitoNEET *in vitro* as demonstrated by photoaffinity labeling (6). In an effort to observe the effects of pioglitazone binding on the protein stability of mitoNEET, we followed the characteristic absorbance of the 2Fe–2S cluster at 460 nm as a function of time at pH 6.0 under conditions known to lead to cluster release (9). The presence of pioglitazone (stoichiometric to the total 2Fe–2S cluster concentration) increased the stability by ≈10-fold compared with the control sample lacking pioglitazone [Fig. 4*A* and supporting information (SI) Fig. 6]. In addition, two-dimensional homonuclear NMR methods (19) demonstrated that, although the overall structure of the protein remains intact upon drug binding, chemical shift changes are observed in the aromatic and aliphatic resonances. NMR resonance(s) of the ring protons of aromatic residues shift and exhibit new through-space couplings upon addition of pioglitazone (Fig. 4*B*). In addition, the amide and ring nitrogen protons of the Tyr-71 and Trp-75 residues are stabilized, leading to slower hydrorogen/deuterium exchange rates (data not shown).

Discussion

Although >650 structures of Fe–S-containing proteins are currently available, the structure of mitoNEET presented here is unique among all known structures (>44,200 structures currently). The 2Fe–2S cluster of recombinant mitoNEET is reversibly reduced/oxidized at pH 8.0 (Fig. 5), consistent with a function for mitoNEET that involves electron transfer. Such functions could include redox reactions with metabolic intermediates, cofactors, and/or proteins localized at the OMM. As mitoNEET regulates maximal respiratory capacity in mouse heart mitochondria (7), it is possible that the protein acts as a sensor, adjusting oxidative capacity through participation in a redox-sensitive signaling pathway.

As intriguing is the unusual lability of the 2Fe–2S clusters in mitoNEET at pH ≤8, attributed to the protonation of the coordinating ligand His-87 (9); His-87 cannot serve as a stabilizing ligand for the 2Fe–2S when protonated. His-87 resides at the N terminus of the helical sequence AHTKHNEET that is predicted to have only marginal helical content in solution (20) but is likely stabilized by cluster binding. Conversely, protonation of the His-87 could destabilize the helix, facilitating cluster release/transfer. A second histidine (His-58) that forms an unusual interprotomer hydrogen bond with Arg-73 (Fig. 3) is also located near the cluster. Disruption of this hydrogen bond would weaken the interprotomer interaction. Because Arg-73 is located sequentially between the Cys ligands of the innermost Fe of the cluster (Fig. 3), perturbation of its inter-

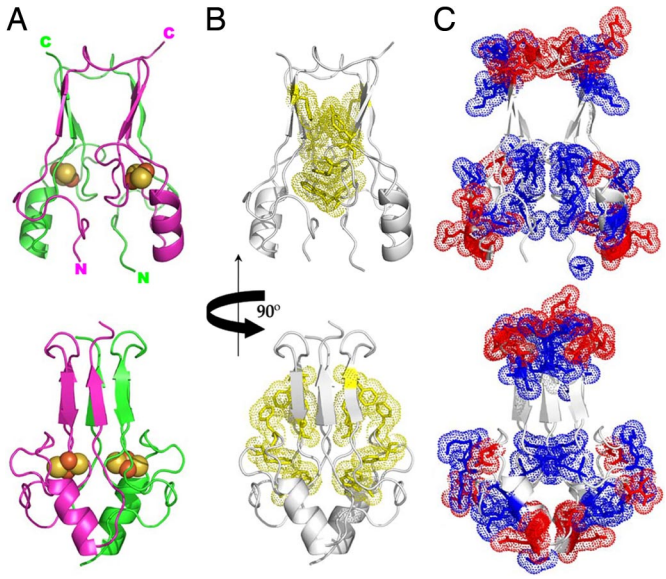

Fig. 2. The overall distribution of charges within mitoNEET creates a macrodipole separated by a hydrophobic belt. (*A*) The ribbon diagram of mitoNEET is displayed in two orientations. The *Lower* view is rotated 90° from the top along the vertical axis shown in the center. The protomers of the unit are colored in green and purple, respectively. Each 2Fe–2S cluster is shown with yellow (sulfur) and red (iron) spheres. (*B*) The ribbons of each protomer are colored gray, and the packing of the 10 aromatic residues (5 from each protomer) are emphasized by yellow dots. Apolar residues are also localized to this region but are not shown. (*C*) The separation of charged residues in mitoNEET indicates segregation of the aromatic and apolar regions of the protein. The negatively charged residues are labeled in red, and the positively charged residues are labeled in blue. The *Upper* panel emphasizes both the asymmetry of charges within the interior of the molecule and the separation of these charges by the nonpolar residues (*B*).

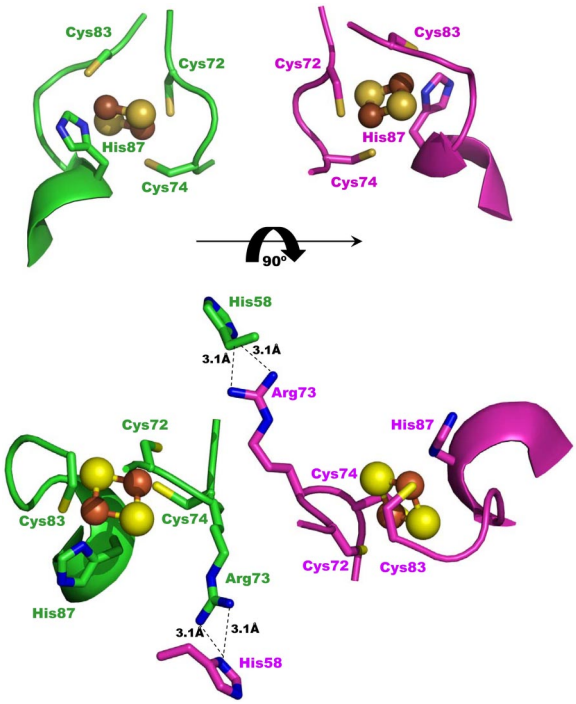

Fig. 3. The 2Fe–2S cluster-binding cradle. (*Upper*) View of the 2Fe–2S cluster (Fe as brown and S as yellow spheres) from a perspective rotated ≈15° from that shown in the *Upper* panel of Fig. 2. The amino acids belonging to the individual protomers are shown in green and magenta. The two 2Fe–2S cradles are related to each other via a 180° rotation along the C_2 symmetry axis of the dimer. Cys-83 and His-87 bind the outermost Fe, whereas the innermost Fe is bound by Cys-72 and Cys-74. The solvent-accessible His-87 is located at the end of the prominent α-helix in the cluster-binding domain (Fig. 1). (*Lower*) View of the cluster cradle rotated 90° clockwise from the view presented in *Upper*. Two additional residues, Arg-73 and His-58, form an unusual His–Arg interprotomer hydrogen bond within the interior of the protein dimer. The distances between the nitrogen of His-58 and the guanidinium nitrogen atoms of Arg-73 are indicated. The two symmetry-related Arg form the positive end of the internal macrodipole (Fig. 2*C*).

action with His-58 will likely lead to reorientation of the inner sphere Cys ligands, potentially providing additional conformational control of binding. Below pH 8 *in vitro*, the 2Fe–2S cluster is labile; the 2Fe–2S cluster is less stable at physiological pH than other 2Fe–2S proteins (9). Modulation of the destabilization/stabilization of cluster binding *in vivo* could be achieved under physiological conditions upon docking of another protein, providing a convenient trigger for controlling cluster release.

This unusual characteristic of the protein raises the interesting possibility that mitoNEET participates in Fe–S cluster assembly, potentially facilitating cluster shuttling between proteins in the mitochondria and cytoplasm. Proteins that act as scaffolds for Fe–S cluster assembly are within the mitochondrial matrix and cytoplasm of yeast and mammalian cells, although matrix synthesis is believed to predominate (14, 21). Although several proteins involved in the export of clusters synthesized in the mitochondrial matrix have been identified in yeast (1, 22), the mechanism by which clusters are transported across the OMM and shuttled to cytosolic apoproteins in yeast and in higher organisms is unknown. MitoNEET is uniquely positioned to possibly receive and then transfer a cluster that has crossed the outer membrane, or alternately may serve as a Fe–S cluster reservoir or storage protein (Fig. 5).

Pioglitazone is a highly hydrophobic molecule that is largely bound to serum albumin after patient ingestion and before cellular uptake and binding to its intracellular targets (23). In addition to hydrophobic interactions, our data indicate that binding of pioglitazone increases stability of the 2Fe–2S cluster and of hydrogen bonding interactions within the protein. Taken together with the unique distribution of hydrophobic residues in the dimer (Fig. 2*B*), our structural results may have important implications for both mechanisms of drug action and future optimization of TZDs. Although these compounds activate peroxisome proliferator-activating receptors, data suggesting alternative modes of action involving mitochondria has accumulated (24). Whether the beneficial effects of TZDs on mitochondria including biogenesis and normalization of lipid oxidation (4, 5) are mediated through mitoNEET is unknown. However, these data, combined with those of Colca *et al.* (6), suggest that pioglitazone can bind and alter the properties of mitoNEET that is expressed in many insulin-responsive tissues (7). Although further biological and biophysical experiments are needed to relate *in vitro* binding to *in vivo* effects, mitoNEET may prove to be an alternative target for drug actions.

Materials and Methods

Construction of Bacterial Expression Plasmid and Purification of MitoNEET. The portion of the human mitoNEET cDNA corresponding to amino acids 33–108 was amplified by PCR and cloned into the pet21a+ vector. Expression in BL21-CodonPlus-RIL and purification was as described (9) with the time after induction extended to 18 h at 22°C. We included an additional cation exchange chromatography step using HiTrap (GE Healthcare) to achieve crystal-quality purification. The purified material had a peak centered at 458 nm and an optical ratio (A_{278}/A_{458}) of 2.3–2.4 under these buffer conditions. Optical spectra were measured on a Cary50 spectrometer (Varian, Walnut Creek, CA).

Pioglitazone Binding. Piogliatzone was solubilized in 0.1 M HCl to a concentration of 3.5 mM. Protein samples containing 15 μM

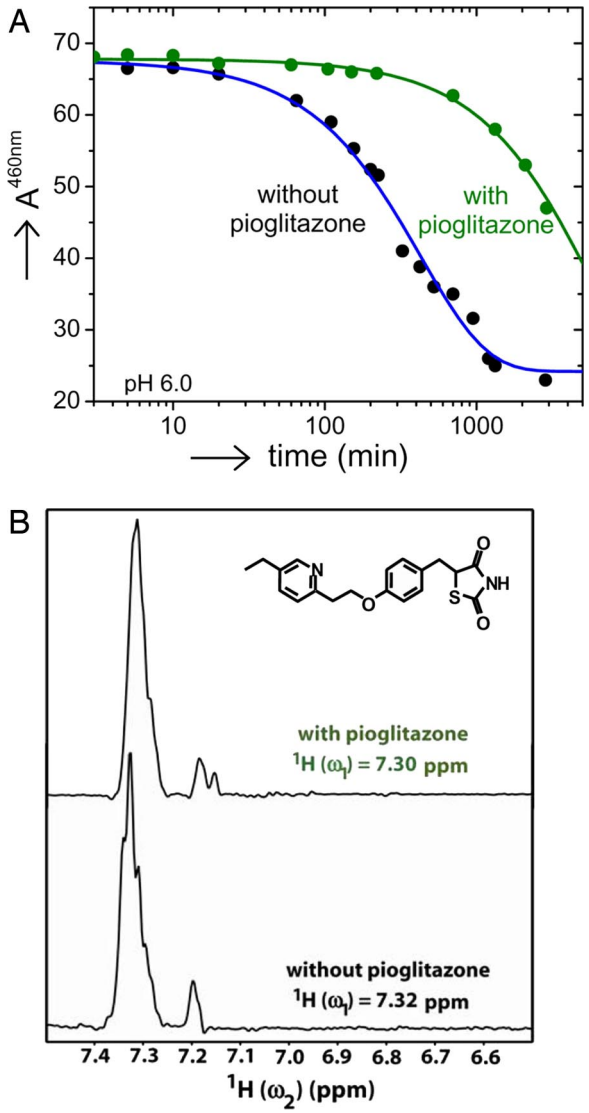

Fig. 4. The binding of pioglitazone to mitoNEET stabilizes the Fe–S cluster. (*A*) The stability of the 2Fe–2S cluster of mitoNEET is increased in the presence of pioglitazone. The change in the signature absorbance spectrum (460 nm) of the 2Fe–2S cluster (oxidized form) was monitored as a function of time at pH 6.0 in the absence and presence of stoichiometric pioglitazone (15 μM). The binding of the insulin-sensitizing drug pioglitazone increased the observed half-life by ≈10-fold. (*B*) 1D vectors derived from 2D homonuclear ^{1}H NOESY spectra of mitoNEET, with and without pioglitazone (D_2O, pH* 7.8, 35°C) are shown. The 1D vectors are along ω_1 at the ω_2 chemical shift typical of the aromatic ring protons of Trp and/or Phe residues.

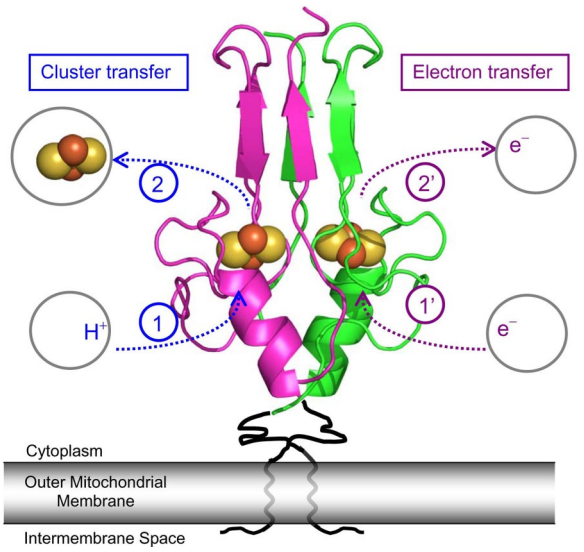

Fig. 5. Possible functional implications of mitoNEET's biophysical properties. MitoNEET is shown linked (magenta and green) to the OMM (gray) (not to scale). On the basis of mitoNEET biophysical properties, two possible functions are suggested: cluster transfer (blue arrows) and electron transfer (wine arrows). Right side (wine), our previous results (9) showed that the 2Fe–2S cluster could be reduced (1′) and reoxidized (2′) (-0.3 V ≤ Em ≤ 0.1 V). Left side, previous and current results showed that upon protonation of His-87 (1), the 2Fe–2S cluster dissociates from the protein (2). We here propose that the changes in the interaction of His-87 with the cluster are likely related to its function. *In vivo* this interaction may be broken by docking of another protein, thereby providing a convenient trigger for cluster release. Binding of pioglitazone to mitoNEET (Fig. 4) increases the stability of the 2Fe–2S cluster, thereby inhibiting release of the cluster.

2Fe–2S centers (7.5 μM dimeric mitoNEET = 15 μM monomeric mitoNEET) were measured in 200 mM phosphate-HCl (pH 7.5) with and without stoichiometric (±10%) pioglitazone (25°C). The stability of the 2Fe–2S clusters was determined from monitoring their characteristic absorbance at 460 nm (λ_{max} at pH 6.0) as a function of time (9). Measurements performed in the NMR buffer (50 mM potassium phosphate/50 mM sodium chloride/5 mM Tris, pH 7.8) gave the same results. The measured pH was the same at the beginning and end of each experiment. Control experiments with equal volume addition of 0.1 M HCl did not change the solution pH (±0.01 units) nor alter the physical and spectral properties (±2%) of the protein.

NMR Spectroscopy. NMR samples of 0.4 mM mitoNEET (protomer concentration) were prepared in 98% D_2O or 90% H_2O/10% D_2O, 50 mM potassium phosphate, 50 mM sodium chloride, 5 mM Tris at pH 7.8. Similar results were obtained in buffers at pH 7.5 and 8.0. Ten microliters of pioglitazone was added in 1-μl incremental amounts to 450 μl of mitoNEET sample. This step was necessary to avoid locally high acidic spots that would destabilize the 2Fe–2S cluster. Following temperature equilibration, NMR spectra were acquired at 36°C by using Bruker DMX 500 MHz and Bruker DRX 600 MHz spectrometers. Homonuclear ^{1}H 2D NOESY spectra were acquired with a mixing time of 400 ms. Spectral processing was performed by using Felix Software (Accelrys, San Diego, CA).

Crystallization. Initial crystallization screening was performed both in house and at Hauptman-Woodward Institute (Buffalo, New York). Screens were attempted around initial conditions that yielded crystals. Our final conditions were 100 mM Tris·HCl (pH 8), 100 mM NaCl , and 30–32% PEG 3000 in the reservoir. Samples were frozen (77 K) after a 1-min soak in 100 mM Tris·HCl (pH 8), 40% PEG3000 and sent frozen (77 K) to SSRL in an SSRL-supplied cassette system for data collection and analysis.

X-Ray Diffraction. Frozen crystals were screened by using the Stanford Automated Mounter (25) operated by Blu-Ice (26). The data were recorded on a 325-mm Marmosaic CCD detector. Data sets were collected from two crystals. A 1.5 Å resolution data set, used for structure refinement, was collected at SSRL BL11–1 from a 0.9- × 0.075- × 0.075-mm crystal. Data were collected from two locations on opposite ends of this crystal by using a 0.1- × 0.075-mm beam size. A three-wavelength Fe-MAD data set, used for initial phasing, was collected at SSRL BL9-2 from a 1.0- × 0.2- × 0.1-mm crystal. The wavelengths for data collection were selected by using a plot of f′ and f″ calculated with the program CHOOCH (27) from the x-ray fluorescence spectrum of the crystal. A total of 360° were

collected at each wavelength following the inverse-beam method with a wedge size of 30°. All data were processed with XDS (28).

Structural Determination. The structure of mitoNEET was determined by MAD phasing (10, 29). Data reduction and primary phasing at a resolution of 2 Å were accomplished by using an automated MAD script developed by Ana Gonzalez (SSRL) that integrates [MOSFLM] (30) and scales [SCALA] (31) the data, phases the structure [SOLVE] (29), and autobuilds a partial model [RESOLVE] (32). Several rounds of automated model-building and refinement were implemented by using ARP/wARP (33), which resulted in significantly improved electron density maps and placement of 97-aa sidechains into electron density.

The data from several independent sets were processed by using an automated script developed by Qingping Xu at the Joint Center for Structural Genomics (JCSG, SSRL) that runs XDS (28). Model completion and refinement were performed in COOT (34) and REFMAC5 (35), respectively. Analyses of the stereochemical quality of the models were accomplished by using an automated validation server developed by Chris Rife at the JCSG (SSRL) implementing MolProbity (12), ADIT (36), and WHATIF 5.0 (37). Structural figures were rendered with PyMol (11).

We thank Christopher L. Rife at the Joint Center for Structural Genomics for providing an automated programming script for coordinate validation and George Feher, Mel Okamura, and Don Blumenthal for many helpful discussions and enthusiastic support. We also thank Hauptman-Woodward Medical Research Institute for initial high-throughput screening experiments. R.N. thanks the Zevi Hermann Shapira Foundation for supporting the collaborative United States–Israeli efforts. This work was supported by that National Institutes of Health [Grants GM 41637 (to M. Okamura), 18024 and 18849 (to J.E.D.), and GM54038 and DK54441 (to P.A.J.)]. Portions of this research were carried out at the SSRL, a national user facility operated by Stanford University on behalf of the U.S. Department of Energy, Office of Basic Energy Sciences. The SSRL Structural Molecular Biology Program is supported by the Department of Energy, Office of Biological and Environmental Research, and by the National Institutes of Health, National Center for Research Resources, Biomedical Technology Program, and the National Institute of General Medical Sciences.

1. Lill R, Muhlenhoff U (2006) *Annu Rev Cell Dev Biol* 22:457–486.
2. Rouault TA, Tong WH (2005) *Nat Rev Mol Cell Biol* 6:345–351.
3. Stark R, Roden M (2007) *Eur J Clin Invest* 37:236–248.
4. Bandyopadhyay GK, Yu JG, Ofrecio J, Olefsky JM (2006) *Diabetes* 55:2277–2285.
5. Bogacka I, Xie H, Bray GA, Smith SR (2005) *Diabetes* 54:1392–1399.
6. Colca JR, McDonald WG, Waldon DJ, Leone JW, Lull JM, Bannow CA, Lund ET, Mathews WR (2004) *Am J Physiol Endocrinol Metab* 286:E252–E260.
7. Wiley SE, Murphy AN, Ross SA, van der Geer P, Dixon JE (2007) *Proc Natl Acad Sci USA* 104:5318–5323.
8. National Center for Biotechnology Information (NCBI) Protein Database, www.ncbi.nlm.nih.gov/sites/entrez?db=protein.
9. Wiley SE, Paddock ML, Abresch EC, Gross L, van der Geer P, Nechushtai R, Murphy AN, Jennings PA, Dixon JE (2007) *J Biol Chem*, 10.1074/jbc.C700107200.
10. Pahler A, Smith JL, Hendrickson WA (1990) *Acta Crystallogr A* 46(Pt 7):537–540.
11. Delano WL, Lam JW (2005) *Abstr Pap Am Chem Soc* 230:U1371–U1372.
12. Lovell SC, Davis IW, Arendall WB, 3rd, de Bakker PI, Word JM, Prisant MG, Richardson JS, Richardson DC (2003) *Proteins* 50:437–450.
13. Holm L, Sander C (1995) *Trends Biochem Sci* 20:478–480.
14. Li K, Tong WH, Hughes RM, Rouault TA (2006) *J Biol Chem* 281:12344–12351.
15. Ramelot TA, Cort JR, Goldsmith-Fischman S, Kornhaber GJ, Xiao R, Shastry R, Acton TB, Honig B, Montelione GT, Kennedy MA (2004) *J Mol Biol* 344:567–583.
16. Colca JR (2006) *Biochem Pharmacol* 72:125–131.
17. Colca JR, Kletzien RF (2006) *Expert Opin Investig Drugs* 15:205–210.
18. Hofmann CA, Colca JR (1992) *Diabetes Care* 15:1075–1078.
19. Wüthrich K (1986) *NMR of Proteins and Nucleic Acids* (Wiley, New York).
20. Muñoz V, Serrano L (1997) *Biopolymers* 41:495–509.
21. Netz DJ, Pierik AJ, Stumpfig M, Muhlenhoff U, Lill R (2007) *Nat Chem Biol* 3:278–286.
22. Lill R, Dutkiewicz R, Elsasser HP, Hausmann A, Netz DJ, Pierik AJ, Stehling O, Urzica E, Muhlenhoff U (2006) *Biochim Biophys Acta* 1763:652–667.
23. Takeda Pharmaceutical Company Limited (2005) ACTOPLUS MET Patient Information Sheet (US Food and Drug Administration Center for Drug Evaluation and Research). Available at www.fda.gov/cder/foi/label/2005/021842lbl.pdf.
24. Feinstein DL, Spagnolo A, Akar C, Weinberg G, Murphy P, Gavrilyuk V, Dello Russo C (2005) *Biochem Pharmacol* 70:177–188.
25. Cohen AE, Ellis PJ, Miller MD, Deacon AM, Phizackerley RP (2002) *J Appl Crystallogr* 35:720–726.
26. McPhillips TM, McPhillips SE, Chiu HJ, Cohen AE, Deacon AM, Ellis PJ, Garman E, Gonzalez A, Sauter NK, Phizackerley RP, *et al.* (2002) *J Synchrotron Radiat* 9:401–406.
27. Evans G, Pettifer RF (2001) *J Appl Crystallogr* 34:82–86.
28. Kabsch W (1993) *J Appl Crystallogr* 26:795–800.
29. Terwilliger TC, Berendzen J (1999) *Acta Crystallogr D* 55:849–861.
30. Leslie AGW (2006) *Acta Crystallogr D* 62:48–57.
31. Bailey S (1994) *Acta Crystallogr D* 50:760–763.
32. Terwilliger TC (2000) *Acta Crystallogr D* 56:965–972.
33. Perrakis A, Morris R, Lamzin VS (1999) *Nat Struct Biol* 6:458–463.
34. Emsley P, Cowtan K (2004) *Acta Crystallogr D* 60:2126–2132.
35. Winn MD, Murshudov GN, Papiz MZ (2003) *Methods Enzymol* 374:300–321.
36. Yang HW, Guranovic V, Dutta S, Feng ZK, Berman HM, Westbrook JD (2004) *Acta Crystallogr D* 60:1833–1839.
37. Vriend G (1990) *J Mol Graphics* 8:52–56.